# Laser-Assisted Additive Manufacturing of mm-Wave Lumped Passive Elements

Ramiro A. RamirezG>, *Student Membe r, IEEE* , Eduardo A. Rojas-NastrucciG, *Member, IEEE* , and Thomas M. WellerG>, *Fellow, IEEE*

*Abstract*- **The performane of additively manufactured microwave passive elements and interconnects continues to improve as better materials, and process techniques are developed. In this paper, laser-enhanced direct print additive manufacturing (LE-DPAM) is used to fabricate capacitors and inductors for coplanar waveguide (CPW) circuits. Acrylonitrile butadiene styrene is used as the dielectric that is printed using fused deposition modeling, and DuPont CB028 conductive paste is deposited using microdispensing. These two techniques are combined with picosecond-pulsed laser machining to achieve 12-µ.m slots on printed conductors, producing aspect ratios greater than 2:1. The same laser is used to fabricate verticalinterconnections that allow for the fabrication of multilayer inductors. Inductances in the range of 0.4-3 nH are achieved, with a maximum quality factor of 21, selfresonance frequencies up to 88 GHz, and an inductance per unit of area of 5.3 nH/mm$^2$. Interdigital capacitors in the range of 0.05-0.5 pF are fabricated, having a maximum1 uality factor of 1000, a capacitance per unit area of 1 pF/mm , and selfresonances up to 120 GHz. All the components are made on the center line of a CPW that is 836-µ.m wide. The results show that LE-DPAM enables the fabrication of compact passive circuits that can be easily interconnected with MMIC dies, which at the same time can be manufactured as pat1 of a larger component. This enables the fabrication of structural electronics that are functional into the millimeter-wave frequency range. Bounds on the inductances and capacitances per unit area are related to material and geometry limitations.**

***Index Terms*- *Additive* manufacturing (AM), laser-enhanced direct print additive manufacturing (LE-DPAM), laser machining, lumped elements, millimeter-wave (mm-wave) passive devices.**

## I. INTRODUCTION

THE number of additive manufacturing (AM) methods that are useful for the fabrica tion of microwave components has grown stead ily in recent years. The size and performance of the AM-produced components are now comparable to or better than those of multilayer, printed circuit board designs thanks to the development of advanced materials and processing techniques. Among the most important advantages of AM are the minimal infrastructure that is required, often involving o nly a single mac hine, and the use of processes that do not require toxic materials such as chemical etchants and photoresist developers. Another key advantage of AM is that it enables dense packaging of IC dies and passives up to millimeter-wave(mm-wave)frequencies. AM can also be used to manufacture conformal circuits and those that are embedded into structures. Components with high inductance and capacitance per unit area, low losses, and high selfresonance frequency (SRF) are main advantages for that AM provides for realizing miniaturized RF front ends.

AM technologies are typically categorized by the material deposition method, each having an associated minimum feature size and layer thickness. Aerosol jet printing (AJP) has been shown to produce passive mm-wave 3-D interconnects with 0.53-dB/mm losses at 40 GHz [1]. By using AJP, the achievable minimum layer thickness, ga p size, and line widths are 0.7, 10, and 10 $\mu m$, respectively. Inkjet printing is another multimaterial technology capable of manufacturing passive components, with a typical drop spacing of 20 $\mu m$ and a layer thickness of 5 $\mu m$ [2], [3]. Inductors with an inductance (L), SRF, and quality factors ( Q) of 7 nH, 4.25 GHz, and 11, respectively, have been achieved with inkjet printing [2].

A third important technology is direct print AM (DPAM) thatcombines fused deposition modeling (FDM) and microdispensing to print dielectrics and the deposit layers of conductive ink or paste. The typical conductor layer thickness and minimum feature sizes that can be achieved with this technology are 30 and 100 $\mu m$, respectively [4]. It has been shown that DPAM can be used to fabricate multilayer RF front e nds at 2.45 GHz [5], [6]. DPAM can also be used for manufacturing conformal 3-D antennas that take the advantage of spherical volumes for improved radiation performance [7], [8]. Pulsed laser machining techniques can be combined with the DPAM process [herein referred to as laser-enhanced or laser-assisted DPAM (LE-DPAM)], to mitigate the effects of edge roughness, tapered line edges and limited minimum feature size that are associated with microdispensing [9], [10]. The laser processing of the conductive paste so lidifies the metal flakes on the edges of a cutting path, creating a high-conductivity region that significantly reduces the ohmic losses

Manuscript received May 3, 2018; revised August 4, 2018 and September 5, 2018; accepted September 14, 2018. Date of publication October 18, 2018; date of current version December 11, 2018. This work was supported in part by the National Science Foundation under Grant ECCSI711790, in part by Sciperio Inc., Orlando, FL 32826 USA, and in part by GGB Industries Inc., Naples, FL 34101 USA. This paper is an expanded version from the IEEE MTT-S 2018 International Microwave Sym posium, June 10- 15, 2018, Philadelphia, PA, USA. *(Correspolldillg author: Ramiro A. Ramirez.)*

R. A. Ramirez was with the Electrical Engineering Departmen,t University of South Florida, Tampa, FL 33620 USA. He is now with QORVO US, lnc., Greensboro, NC 27409 USA (e-mail: ramiror@mail.usf.edu).

E. A. Rojas-Nastrucci is with the Electrical, Computer, Software, and Systems Engineering Department, Embry-Riddle Aeronautical University, Daytona Beach, FL 32114 USA (e-mail: eduardo.rojas@erau.edu).

T. M. Weller is with the School of Electrical Engineering and Computer Science, Oregon State University, Co rvallis, OR 97330 USA (e-mail: tom.weller@oregons tate.edu).

Color versions of one or more of the figures in this paper are available online at http://ieeexplore.ieee.org.

Digital Object Identifier 1O.l 109/f MTT.2018.2873294

for coplanar waveguide (CPW) interconnects [10]. Among other demonstrations, LE-DPAM has been used to manufacture low-loss packaging and interconnection of MMIC dies [11], high-Q filters and resonators [12], and mm-wave multilayer interconnects [13].

In this paper, the fabrication process, measurements, and modeling of CPW capacitors, and multilayer inductors are described. The LE-DPAM process is used to fabricate multilayer spiral inductors and interdigital capacitors (IDCs), where microdispensed silver ink (Dupont CB028) is used as the conductor, acrylonitrile butadiene styrene (ABS) is used for the dielectric layers [14], and picosecond-laser processing is employed to machine the features on the conductive ink layers. This paper is an extended version of [15], where results on the fabrication and measurements of the IDCs are presented. The current version of the paper includes the circuit modeling of the capacitors, as well as the fabrication, characterization, and circuit modeling of the spiral inductors. Analytical design equations and curves for both the inductors and the capacitors, and a study of the main sources of dissipative losses in the components have also been added in this extended paper.

Results show that capacitances in the range of 0.05--0.5 pF are achieved at 30 GHz, with $Q$ factors up to 1000 and selfresonant frequencies above 120 GHz. On the other band, inductance values in the range of 0.4-3 nH, with quality factors up to 21 and selfresonance frequencies up to 88 GHz, are achieved. To the best of the authors' knowledge, this is the first time that it is shown that LE-DPAM can be effectively used to fabricate mm-wave passive components with dimensions and reactance values that are useful for front ends with $Q$ factors that approach the values obtained with the multilayer laminates that are commonly used in industry. Such AM components can be used for the fabrication of **MMIC** packaging, conformal antennas, and filters, all supporting emerging uses of the mm-wave frequency spectrum.

## II. GENERAL FABRICATION PROCESS

The components in this paper are fabricated using a multilayer LE-DPAMprocess that involves interleaving FDM steps for dielectric deposition with microdispensing steps for conductor deposition. The substrate dielectric is the ABS, which has a relative permittivity of 2.35 and a loss tangent of 0.0065 (measured at 30 GHz) [14]. The vertical interconnections between the layers are achieved by laser machining the ABS and filling the cavities using microdispensing of DuPont CB028, a silver paste with a reported de bulk conductivity of 0.76 x $10^6$ $Sim$ when dried at 90 °C [16]. The complete via fabrication process is described in [13].

The fabrication process starts with a printing bed that is heated to 90 °C. ABS is printed using **FDM**, as shown in Fig. l(a), by extruding with a ceramic tip at a temperature of 235 °C. The tip's inner diameter is 75 $\mu m$, which allows ABS to be printed in layers that are 50-$\mu$m thick. The first conductive layer is printed on the ABS using microdispensing [see Fig. 1 (b)], with a printing height (the distance from the tip to

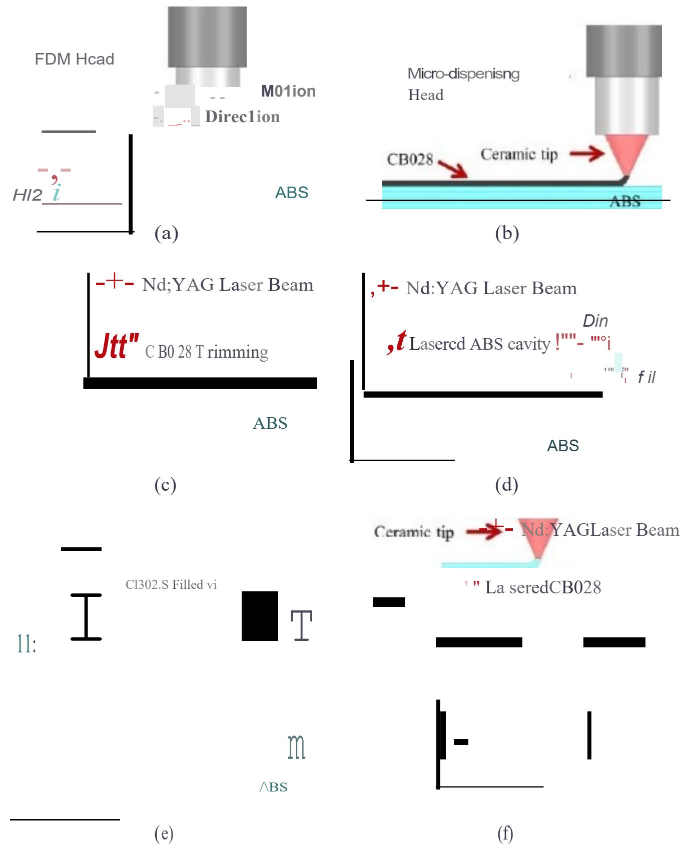


the substrate during printing), air pressure, and printing speed of 70 $\mu m$, 12 psi, and 25 mm/s, respectively. The thickness

Fig. I. LE-DPAM process used to fabricate the inducto rs. (a) ABS substrate deposition through FDM with a total height of $H/2 = 150$ *pm.* (b) CB028 microdispensing of under pass with a typical ink thickness :::'. 30--60 *pm.* (c) Picosecond-laser trimming of CB028. (d) After a second ABS layer is deposited, laser processing is utilized to machine $H2 = 150$ *pm* deep cavities in the ABS. (e) Cavities filled with CB028 to form con- ducting vias. (f) Laser trimming is used to pattern the final element geometry.

of the resulting CB028 conductive layer varies approximately from 30 to 60 $\mu m$. This first conductive layer is then machined using a Lumera SUPER RAPID-HE picosecond laser, with a wavelength, scanning speed, average power, and repetition rate of 1064 nm, 25 mm/s, 2.4 W, and 100 **KHz,** respec- tively, to achieve the geometry needed for an interconnect [see Fig. l (c)]. ABS is printed again, covering the conductive

traces, and laser machining is used to machine the via cavities as shown in Fig. l(d). For this step, the laser average power is changed to 0.8 W, for an accurate and controlled etch rate. The cavities are then filled using microdispensing as shown in Fig. l(e). A final conductive layer is deposited using microdispensing, and the laser is used to machine the slots required to realize the inductor [see Fig. l(f)]. This process is also used to fabricate the IDCs. Note that the capacitors in this paper do not require the steps to fabricate the via.

Fig. 2(a) depicts the typical profile of a via with a dimen- sions of around 200 $\mu m$ x 200 $\mu m$ x 150 $\mu m$, measured with a Dektak Dl 50 profilometer.

To accurately predict the depth of the cavities, the etch rate for CB028 and ABS as a function of the number of laser passes is calculated as shown in Fig. 2(b), using an average laser power of 0.8 W. The etch rates are around 5 µm/pass and 8 µm/pass for CB028 and ABS, respectively.

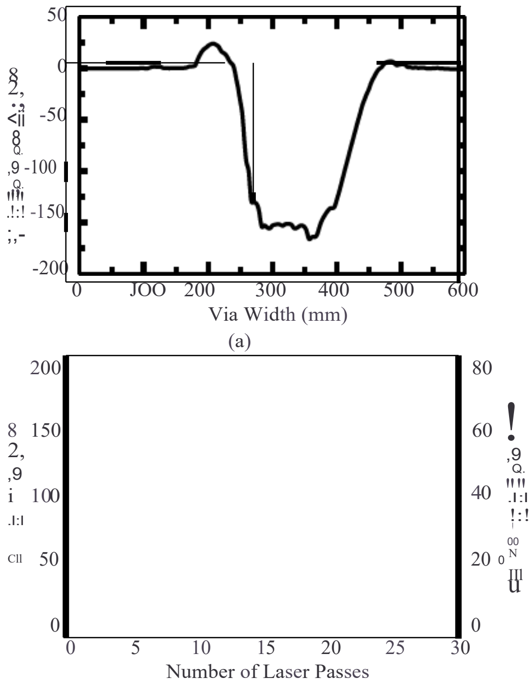


Fig. 2. (a) Profile of a via cavity. (b) Etch depth for ABS and CB028 as a function of the number of passes for a laser power of 0.8 W.

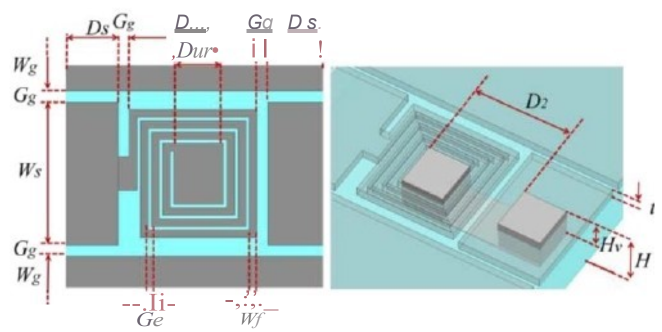


Fig. 3. (a) Top view of the proposed spiral inductor geometry. (b) RF signal via separation and heights.

### III. SPIRAL INDUCTORS

Following the fabrication procedure introduced in Section II, different spiral inductors are presented with characterization data up to 30 GHz. Simulated, modeled, and measured data are shown to demonstrate the feasibility and control of the proposed process.

#### *A. Design and Fabricated Prototypes*

The geometry of the inductor is a spiral that is patterned inside the center conductor of a CPW, as shown in Fig. 3(a) and (b). The center of the spiral is connected to the output port by using a buried bridge or underpass and two vertical vias. A set of four inductors with different numbers of turns $N$ of 0.5, 1, 2.5, and 3 are designed and fabricated to demonstrate the described fabrication technique. The linear size of these elements is designed to be much smaller than the guided wavelength (i.e., < *Agl8)* at the desi red

TABLE I

SPIRAL INDUCTOR GENERAL D IMENSIONS

| N° of Turns *(N)* | 0.5 | | 2.5 | 3 |
|---|---|---|---|---|
| *D••,( )lill)* | 340 | 470 | 600 | 750 |
| D,.(µm) | 200 | 272 | 200 | 290 |
| *D,* (µm) | 450 | 498 | 602 | 657 |

The following variables remain unchanged for all designs. *W,* = 834.6 µm; $G_8$= 65 µm; *Wg* = 2 mm, *W.F*46 µm; *D,*= 520 µm;, *G* "' 12-15 µm; *t* "' 30-60 µm; *H*= 300 µm; ,*H* = 150 µm.

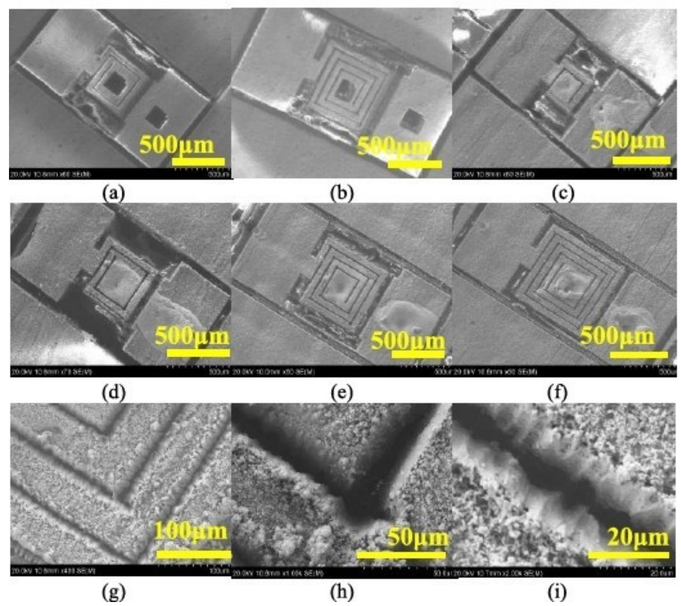


Fig. 4. (a) and (b) SEM image of 0.5 and I turn inductors with via holes. (c}-(f) Top view of the fabricated inductors with different number of turns *(N* = 0.5,, I 2.5, and 3). (g}-(i) Close-up images of the machined slots and windings.

frequency range, taking into the account of design drivers such as the selfresonant frequency, quality factor, and effective series inductance. The dimensions of the fabricated samples are listed in Table I.

Fig. 4 shows the top views of the fabricated spiral inductors. The SEM micrographs of two inductors with nonfilled vias are included in Fig. 4(a) and (b) to indicate their location in the geometry. Fig. 4(c)-(f) shows fabricated inductors with different numbers of turns *(N* = 0.5, 1, 2.5, and 3). The details of the machined windings and slots are depicted in closeup images in Fig. 4(g)-(i), where gaps with dimensions '.::::'.12 - 15 *µm* are observed , creating 2:1 aspect ratio cuts.

#### *B. Measured and Simulated Results*

The results in this work were obtained using HFSS 17.1 for the 3-D EM simulations and Keysight Advanced Design System 2016.01 for circuit modeling. Measured data were obtained with an Agilent PNA-N5227A, a JMicroTech Jr-2727 probe station, and *650-µm* GGB picoprobes. Fig. 5(a) shows the measurement setup, and Fig 5(b) shows a closeup view of the on-board probing of the fabricated devices.

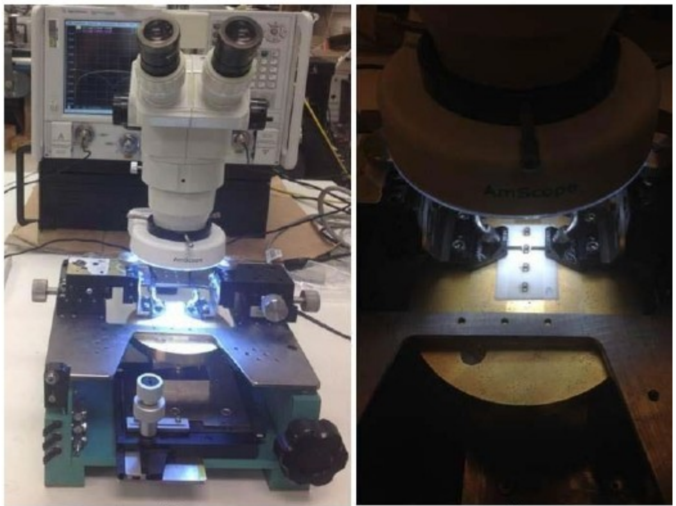

(a) (b)

Fig. 5. (a) Measurement setup. (b) Close-up of on-board probing.

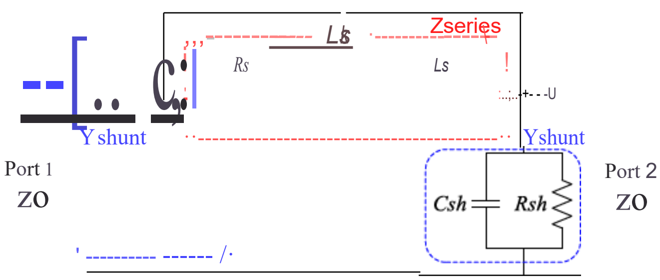


Fig. 6. Spiral inductor equivalent circuit model.

The performance of the fabricated spiral inductors can be modeled using the RLC equivalent circuit model shown in Fig. 6 [17]- [19]. The parameter *Ls* describes the main selfinductance of the device, which is proportional to the total length of the strip line that creates the spiral and the number of turns *N*. The parameter *Rs* describes the low-frequency ohmic losses across the inductor, and an additional parallel *Ls* κ and *Rs*κ model the frequency-dependent skin and proximity effects. *Cg* accounts for the parasitic capacitive coupling within the spiral winding, a value heavily affected by the CB028 thickness *t* and the gap *Ge* between different turns.

Finally, Csh and Rsh represent the parasitic capacitance of the spiral winding to ground, and substrate loss, respectively.

From the two-port inductor model presented in Fig. 6, the series impedance Zseries can be given as follows:

$$Z_{series}(\omega) = [R_{series}] + j\omega \cdot [L_{series}](\Omega) \quad (1)$$

$$Z_{series}(\omega) = \left[R_s + \frac{\omega^2 L_{sk}^2 \cdot R_{sk}}{\omega^2 L_{sk}^2 + R_{sk}^2}\right] + j\omega\left[L_s + \frac{R_{sk}^2 \cdot L_{sk}}{\omega^2 L_{sk}^2 + R_{sk}^2}\right]. \quad (2)$$

From the Y-equivalent circuit of a reciprocal two-port 1r-network [20], the parallel value of Zseries and the capacitive reactance provided by *Cg* can be given as follows:

$$Z_{series}(\omega) // \frac{1}{j\omega \cdot C_g} = \left[-\frac{1}{Y_{21}}\right]. \quad (3)$$

Therefore, at frequencies, where the effects of *Cg* are negligible, Zseries can be approximately equal to the following equation:

$$Z_{series}(\omega) \cong \left[-\frac{1}{Y_{21}}\right]. \quad (4)$$

The value of the resistance *Rs* can then be extracted from the measured S-parameters, since its value is approximately equal to the measured series resistance Rseries at low frequencies. As given by

$$\mathrm{Re}\left[-\frac{1}{Y_{21}}\right] \cong \mathrm{Re}[Z_{series}(\omega)] \cong R_{series} \cong R_s. \quad (5)$$

Similarly, the value of the effective inductance Lseries can be extracted from the measured S-parameters to provide an initial estimate of the value of *Ls* + *Lsk* as given by

$$\mathrm{Im}\left[-\frac{1}{Y_{21}}\right] \cong \mathrm{Im}[Z_{series}(\omega)] \cong \omega L_{series} \cong \omega(L_s + L_{sk}). \quad (6)$$

Likewise, from the Y-equivalent circuit of a reciprocal two-port π-network [20], the value of Yshunt can be given as

$$Y_{shunt}(\omega) = [Y_{11} + Y_{12}](\mho). \quad (7)$$

Initial estimates for the shunt admittance can then be given as

$$\mathrm{Re}[Y_{11} + Y_{12}] = \mathrm{Re}[Y_{shunt}(\omega)] \cong \frac{1}{R_{sh}}(\mho) \quad (8)$$

$$\mathrm{Im}[Y_{11} + Y_{12}] = \mathrm{Im}[Y_{shunt}(\omega)] \cong \omega C_{sh}(\omega). \quad (9)$$

Using these initial estimates, the circuit model values are subsequently obtained through optimization and curve fitting in Keysight ADS to match the measured S-parameter data. The complete set of extracted values for different number of turns *N* is listed in Table II.

TABLE II
SPIRAL INDUCTOR EQUIVALENT CIRCUIT MODEL VALUES

| Parameter | N=0.5 | N=1 | N=2.5 | N=3 |
|---|---|---|---|---|
| Rs(11) | 0.45 | 2.16 | 2.866 | 2.98 |
| Rsk (11) | 3.01 | 3.8 | 4.11 | 8.02 |
| Ls,(nH) | 1.1 | 1.1 | 1.1 | 0.4 |
| C, (IF) | 10.2 | 21.5 | 44.1 | 54.2 |
| Ls (nH) | 0.399 | 0.879 | 1.582 | 2.24 |
| Cs• (fF) | 35.06 | 35.12 | 38.02 | 39.13 |
| Rs.(Jill) | 5.5 | 5.5 | 5.5 | 5.5 |

Fig. 7 shows the measured, modeled, and EM-simulated S-parameter data up to 30 GHz for the fabricated spiral inductors with different numbers of turns. There is a good agreement between the measured and simulated data, indicating a high degree of process control and simulation accuracy.

For the same fabricated devices, Fig. 8(a) shows the simulated, modeled, and measured inductance over frequency, computed from (10), where values of 0.4 nH (for $N = 0.5$)

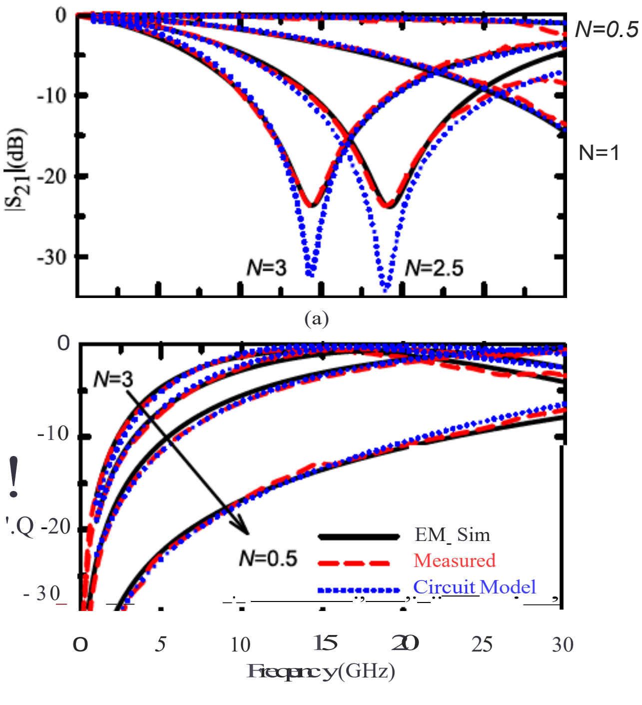


Fig. 7. Measured, simulated, and modeled (a) transmission coefficient and (b) reflection coefficient of four spiral inductors fabricated with LE-DPAM.

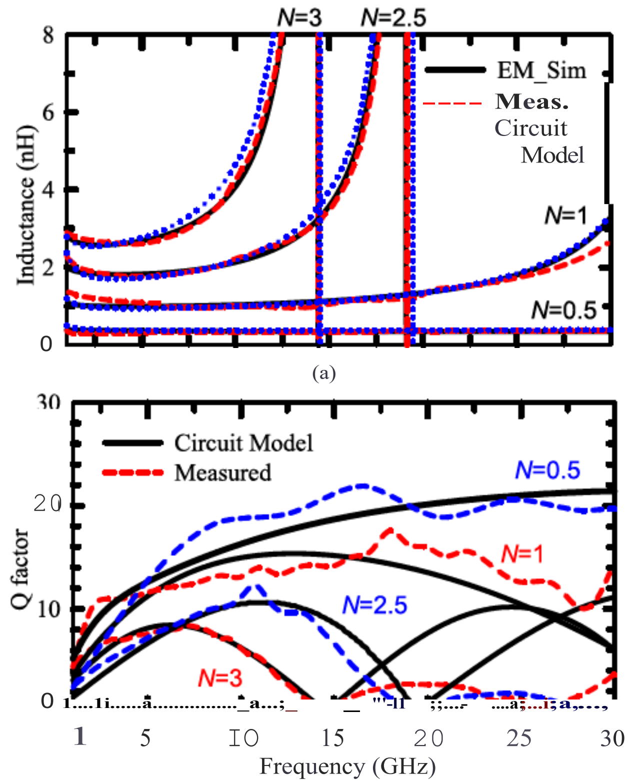


Fig. 8. Measured, simulated, and modeled (a) inductance and (b) quality factor for spiral inductors with different numbers of turns.

and 2.87 nH (for $N = 3$) are achieved at 5 GHz; similarly, values of 0.46 **nH** (for $N = 0.5$) and 2.70 nH (for $N = 1$) are achieved at 30 GHz. Close agreement between the measured and simulated data is also observed here

$$L(m) = \frac{1\times10^{9}}{\omega(d)} \operatorname{Im}[-Y_{21}(b)]\ (\mathrm{nH}). \qquad (10)$$

Fig. 8(b) shows the measured and simulated quality factor (Q) computed from (11). The measured $Q$ values are extracted from the measured two-port S-parameters

$$Q = \frac{\operatorname{Im}\{-1/Y_{21}\}}{\operatorname{Re}\{-1/Y_{21}\}}. \qquad (\ )$$

Maximum $Q$ values vary in the range of 8.4, 10, 15.6, and 21 for spiral inductors with $N = 3$, 2.5, 1, and 0.5, respectivel.y It is seen from Fig. 8(b) how this maximum value occurs at different frequencies, depending on the ratio of parasitic reactance and the series selfinductance $Ls$. The $Q$ value decreases at higher frequencies when the equivalent parasitic capacitive reactance is dominant in the circuit, until reaching a zero value at resonance [17].

To understand the main sources of loss in the inductor and the limitations of the geometry, the quality factor (Q) versus conductivity of the metal layer and loss tangent (tani5) of the substrate are extracted from simulations. Results show that variation in tani5 from 0.02 (FR4) to 0.0009 (Zeonex) [21] causes only a 5% change in $Q$. On the other hand, the conductivity has a greater effect on the quality factor, as shown in Fig. 9.

Based on the measured $Q$ values, the effective conductivity of the laser machined CB028 is in the range of 4.6 MS/m,

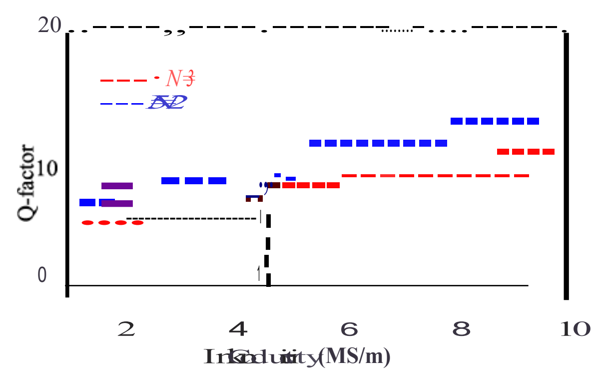


Fig. 9. Quality factor plotted against ink conductivity for $N = 2.5$ and 3.

which is better than the typical 0.76-MS/m de conductivity of CB028 when dried at 90 °C. This suggests that the laser processing improves the performance of the inductor. Note that for a 10-MS/m conductivity, simulations show that the $Q$ values would be in the range of 13.8 and 11.4 for this particular geometry with $N = 2.5$ and 3, respectively.

The first SRF was calculated using a set of EM-simulated results, to determine the effective operational frequency range of the devices. Fig. lO(a) shows the value of the SRF for variations in the number of spiral turns $N$, obtaining values of 88 and 15 GHz for $N = 0.5$ and 3, respectively.

Fig. lO(b) shows the predicted changes in effective inductance for variations in the number of turns $N$. These changes are computed through a simple yet accurate analytical equation (12) that has been modified from the ones presented in

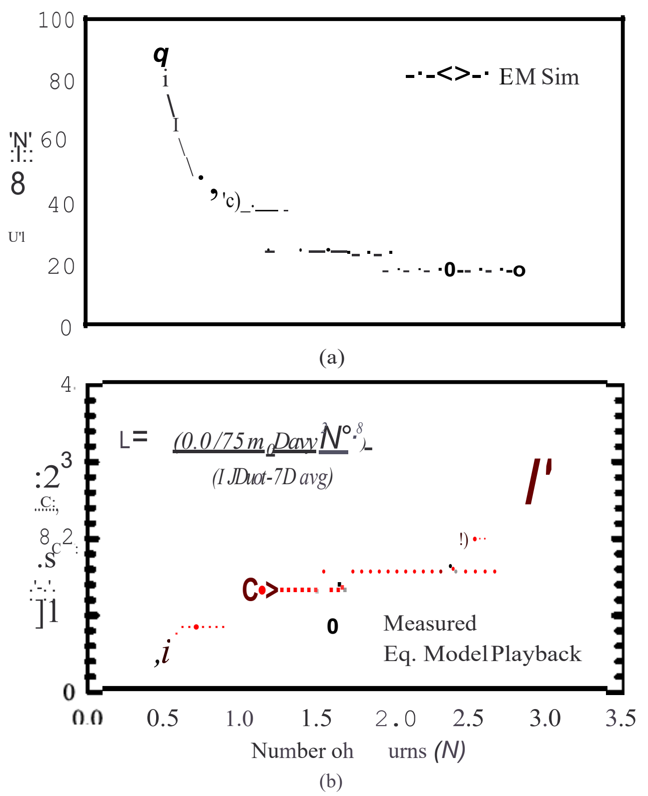


(a)

(b)

Fig. JO. (a ) Spiral inductor SRF. (b) Equation-based prediction of inductance plotted against the number of turns *N*.

[19], [22], and [23] that were originally introduced to calculate the inductance in rectangular s pirals

$$L = \frac{0.0175 \cdot \mu_0 \cdot D_{avg}^2 \cdot N^{0.8}}{11 \cdot D_{out} - 7 \cdot D_{avg}} \quad \textbf{(nH)} \qquad (12)$$

where Dout (m) is the outer diameter as shown in Fig. 3(a) and Davg (m) is the arithmetic mean between the inner $D_{in}$ (m) and outer coil diameter. The equation is optimized specifically for the proposed technology (i.e., LE-DPAM) utilizing CB028 and ABS as a conductive ink and a dielectric substrate, respectively, and has been modified to fit measured and simulated values taken at the center frequency of the operational bandwidth established by the SRF. This approach results in a difference of less than 5% from the near de inductance value. A very good agreement is observed between the equation model playback and the obtained inductance values, ranging from 0.4 to 2.9 nH, with a maximum error of 5.6%.

Table III shows a comparison of measured performance with previously published related work, including different geometries and fabrication technologies. Note that AM inductors tend to have lower *Q*, when compared with the ones obtained from GaAs dies. The main reasons for this are the lower conductivity of the metals and the high tan /J of the printed dielectrics. In this paper, higher *Q* values are achieved when compared with other AM devices due to the use of laser machining, which increases the effective conductivity of the silver paste [10]. The devices presented here perform similar to traditional multilayer circuit boards.

TABLE ill

COMPARISON WITH PREVIOUSLYPUBLISHED WORK

| Work | Process | Inductance (nH) | SRF (GHz) | Q.,.. | Inductance per unit Area nH/mm$^2$ |
|---|---|---|---|---|---|
| [2] | Ink jet | 7 | 4.25 | 11 | 1.47 |
| [24] | Liq. Metal | 92 | 0.71 | 24 | 0.9 |
| [3] | Inkjet | 75/9.7 | 0.2/0.8 | 3/4 | 1.8/0.8 |
| [25] | LTCC | 7.15 | 2.33 | 33.5 | I.I |
| (26] | GaAs | 0.7/2.8 | 9/24 | 16/22 | 20/31 |
| This Work* | LEDPAM | 0.4/3 | 88/15 | 8.6/21 | 4.3/5.3 |

*LEDPAM = laser enhan ced direc t print addit ive manufacturing

TABLE IV

IDC GENERAL D IMENSIONS

| N° of F ingers *(NF)* | 3 | 7 | 9 | 11 | 13 |
|---|---|---|---|---|---|
| *WF( μm)* | 264.8 | 102 | 74.9 | 57.6 | 45.7 |

The following variables remain unchanged for all designs: *Ws* = 834.6 μm, *G* = 65 μm; *W* = 2 mm; *D*, = 520 μm; *G* "' 12- 15 μm; 30-6 0 μ m ; *h* = 300 μ m. Mul tiple finge r length s *(D n )* we re studi ed an d wi ll be indicated as need ed in the plot s.

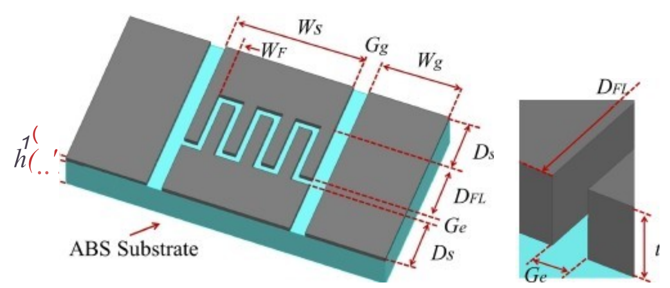


Fig. 11. Proposed CPW JDC geometry.

## I V. I NTE RDI GITA L CAPACITORS

The LE-DPAM process is also utilized for the realization of high-performance lumped CPW IDCs, elements that can be integrated with matching, filtering, or biasing networks and fabricated in a single-layer process as shown in Fig. l(a)- (c). In this section, several IDCs are presented, characterized, and compared with previous related work up to 30 GHz. The content in this section includes results shown in [15] that are used to propose and validate a circuit model.

### A. Design and Fabricated Prototypes

As in Section ill , where spiral inductors were introduced, some of the critical parameters that are often considered as drivers in a lumped passive element design include the overall size, SRF, quality factor, and effective series capacitance. Fig. 11 shows the proposed IDC geometry, and Table IV includes all the general dimensions for the different capacitors fabricated.

Effective capacitances in the range of 0.05- 0.5 pF at 30 GHz are achieved by changing the finger length (DFL), Fig. 12(a)-(d) shows the fabricated IDC prototypes with different finger lengths and Fig. 12(e)-( f) shows typical laser

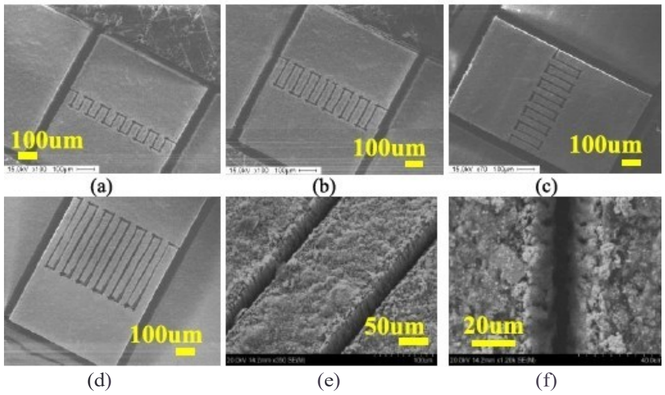


Fig. 12. (a}-{d) SEM images of IDC for different finger lengths (DFL = 100, 200, 300, and 500 $\mu m$). (e) SEM image of a laser cut with a 2:1 AR. (f) Close-up SEM image of a typical laser cut on a CB028 slot width 12- 15 ;,m and a paste thickness 30----60 $\mu m$_ Number of fingers NF = 13.

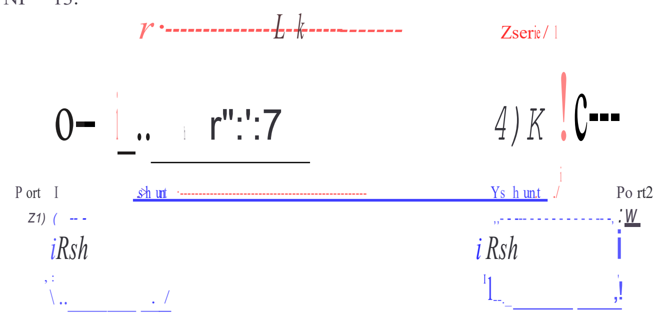


Fig. 13. IDC equivalent circui t model.

cuts in a 2:1 aspect ratio. All fabricated devices have a fixed number of fingers NF eq ual to 13_

### *B. Measured and Simulated Results*

T he performance of the fabricated devices is emulated using the lumped element model in Fig. 13. The parameter *Cs* describes the main electric coupling between the fingers produced by the series capacitance of the device. The value for *Cs* is proportional to the total length of the fingers DFL, number of fingers NF, and thickness of CB028 *t*. The parameters Csh and Rsh represent the parasitic capacitance of the input-o utput interdig ital structure to ground and the substrate loss, respectively. The two inductors *Ls* and mutual inductive coupling factor *K* accou nt for the parasitic magnetic coupling between the fingers. Finally, the parameter *Rs* describes the low-frequency ohmic losses across the capacitor, and an additional parallel *LsK* and *RsK* model the frequency-dependent skin and proximity effects.

From the circuit model in Fig. 13 and at frequencies where the effects of *Ls* are negligible, Zseries can be approximately equal to (13) and (14)

$$Z_{series}(w) = [R_{series}] + j \cdot \left[ -\frac{1}{w \cdot C_{series}} \right] \quad (\Omega) \tag{13}$$

$$Z_{series}(w) = \left[ \frac{1}{2}\left( R_s + \frac{w^2 \cdot L_{sk}^2 \cdot R_{sk}}{\omega^2 L_{sk}^2 + R_{sk}^2} \right) \right] + j\left[ \frac{1}{2}\left( -\frac{1}{\omega \cdot C_s} + \frac{\omega \cdot R_{sk}^2 \cdot L_{sk}}{w^2 \cdot L_{sk}^2 + R_{sk}^2} \right) \right]. \tag{14}$$

TABLE V

JDC EQUIVALENT C IRCUIT MODEL VALUES

| Parameter | 100 µm | 200 µm | 300 µm | 400 µm | 500 µm | 600 µm |
|---|---|---|---|---|---|---|
| *Rs* (n) | 1.02 | 1.02 | 1.09 | 1.12 | 1.14 | 1.16 |
| RsK(n ) | 4.2 | 4.11 | 4.1 | 8.8 | 9.82 | 10.6 |
| LsK(nH) | 0.35 | 0.3 | 0.21 | 0.19 | 0.07 | 0.07 |
| *RsH(k n )* | 5.5 | 5.5 | 5.5 | 5.5 | 5.5 | 5.5 |
| *Cs* (pF) | 0.034 | 0.048 | 0.065 | 0.084 | 0.104 | 0.125 |
| Ls (nH) | 0.ot | 0.04 | 0.12 | 0.130 | 0.151 | 0.183 |
| *C,h* (pf) | 0.005 | 0.005 | 0.030 | 0.042 | 0.045 | 0.048 |
| ***K*** | 0.52 | 0.55 | 0.68 | 0.68 | 0.69 | 0.7 |

Variations for different finger length *DFL*, ***K*** = mutual inductor coupling coefficient. Number of fingers *NF*= 13.

From the *Y* -equivalen t circ uit of a reciprocal two-port ir-network [20], the value of Zseries can be given as

$$Z_{series}(w) = \left[ -\frac{1}{Y_{21}} \right]. \tag{15}$$

An estimate value of the series resistance *Rs/2* can then be extracted from the measured S-parameters, since its value is approximately equal to the measured series resistance Rseries at low frequencies. As given by

$$\mathrm{Re}\left[ -\frac{1}{Y_{21}} \right] = \mathrm{Re}[Z_{series}(w)] = R_{series} \cong \frac{R_s}{2}. \tag{16}$$

Similarly, the value of the series capacitance Cseries can be extracted from the measured S-parameters to provide an initial estimate for *Cs* at low freq ue ncies as given by

$$\mathrm{Im}\left[ -\frac{1}{Y_{21}} \right] = \mathrm{Im}[Z_{series}(w)] = \frac{-1}{w \cdot C_{series}} \cong \frac{-1}{2 \cdot w\, C_s}. \tag{17}$$

I n ad dition , from the Y-eq uivalent circuit of a reciprocal two-port ir-network [20], the value of Yshunt can be given by

$$Y_{shunt}(w) = [Y_{11} + Y_{12}]\,(\,). \tag{18}$$

From the model in Fig. 6, initial estimates for the shunt admittance can then be given by

$$\mathrm{Re}[Y_{11} + Y_{12}] = \mathrm{Re}[Y_{shunt}(w)] \cong \frac{1}{R_{sh}(w)} \tag{19}$$

$$\mathrm{Im}[Y_{11} + Y_{12}] = \mathrm{Im}[Y_{shunt}(w)] \cong \omega C_{sh}(w). \tag{20}$$

The exact circuit model values, as in the previous section, are obtained through circuit optimization and curve fitting in Keysight ADS to match the measured S-parameter data. The final parameter values are listed in Table V.

T he simulated and measured reflection and transmission coefficient results of IDC with NF = 13 and different finger lengths (DR) areshownin Fig. 14[15].The effective capacitance of the component is computed using (21), and shown in Fig. 15(a), achieving 0.05 and 0.25 pF at low frequencies for DR = 100 and 600 $\mu m$, respectively,

$$C(w) = \frac{-1 \times 10^{12}}{\mathrm{Im}\left[ -\frac{1}{Y_{21}} \right] \cdot \omega} \quad (\mathrm{pF}). \tag{21}$$

Fig. 15(b) shows the simulated and measured $Q$ factor, computed using (11). The measured $Q$ values are, as in

TABLE VI
COMPARIS ON WITH PREVIOUS P UBLISHEDWORK

| Work | Geometry | Process | $Q_{max}$ | Capacitance per unit Area ( F/ mm$^2$ | SRF max (GHz) |
|---|---|---|---|---|---|
| This work | Interdigital | LEDPAM | 1000 | 0.99 | 120 |
| [27] | lnterd-mom | GaAs | 400 | 22.5 | >120 |
| [2] | MIM | Inkjet | 15 | 6.5 | 2.5 |
| [2] | **MIM** | Coppe r | 35 | 1. 2 5 | |
| [2 8] | **MIM** | GaA s | 10 00 | 105 | 1 1.5 |
| [3 ] | **MIM** | Inkjet | 12.9 | 48.2 | 1.3 |

LE DPAM: laser enhanced direct print additive manufacturing.

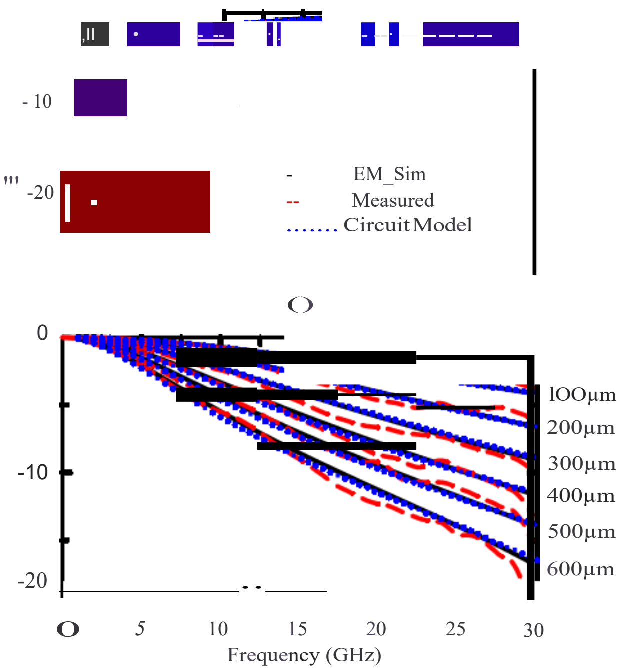


(b)

Fig. 14. Measured, simulated, and modeled (a) transmission coefficient and (b) reflection coefficient of several IDCs with different finger length DFI., (noted in the plot) fabricated with LE-DPAM. Number of fingers NF = 13.

the previous section, extracted from the measured two-port S-parameters while simulated values are obtained from the equivalent RLC circuit model presented in Fig. 13.

A set of EM simulated design curves that show the behavior of the first SRF was studied to determine the effective operational frequency range of the devices. Fig. 16(a) shows the value of the SRF for variations in the number of fingers NF and finger length *DFI,* obtaining values ranging from 20 to 120 GHz.

Fig. 16(b) shows the predicted changes in effective capacitance for variations in the number of fingers NF and finger length D FL· These changes are computed through (22)-{25), an analytical equation modified to fit the proposed technology

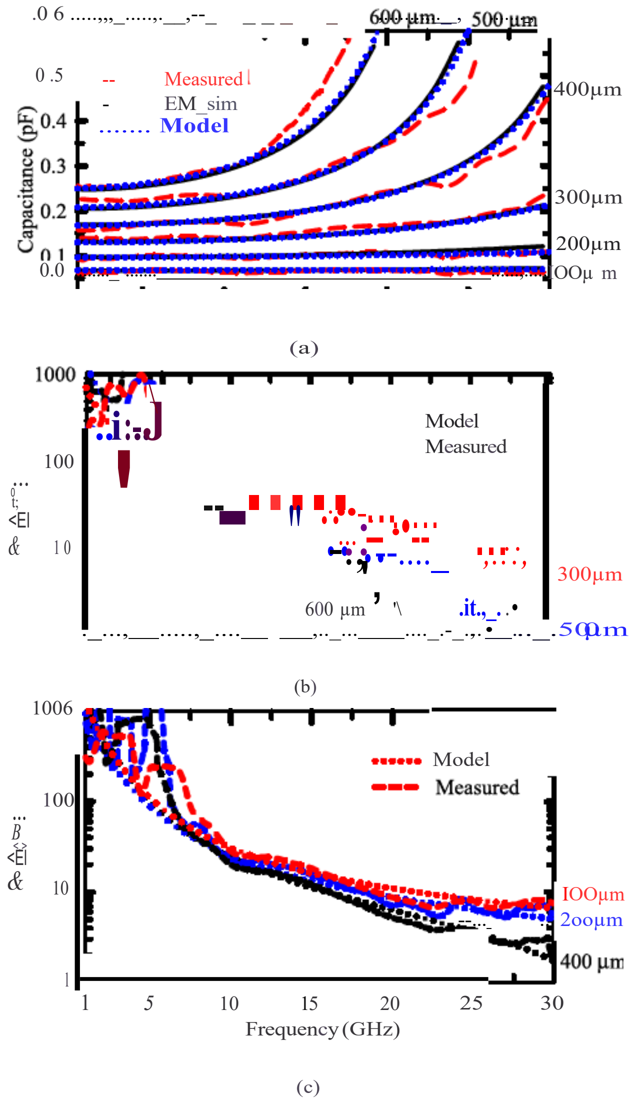


Fig. 15. Measured, simulated, and modeled (a) capacitance for devices with different *DFL* and (b) and (c) quality factor for IDCs with different finger lengths DFI.,(noted in the plot). Number of fingers NF= 13.

from the well-known parallel plate capacitance equation [23].

$$C = C_1 \cdot \varepsilon_0 \cdot \varepsilon_r \cdot \frac{t}{\ldots} \quad \text{(pF)} \tag{22}$$

$$C_1 = 0.691 - (0.014 \cdot NF) \tag{23}$$

$$W_F = \frac{(W_S - G_e \cdot (NF - 1))}{NF} \tag{24}$$

$$D_I = (VFL \cdot (NF - 1) + (W_F \cdot NF)) \tag{25}$$

where $C_1$ represents a proportionality constant, $W_F$ depicts the finger width, NF the number of fingers, *Ge* the gap between the interdigital structures, $D_I$ the total overlapping interdigital distance, and *t* the ink thickness as shown in Fig. 11. As in Section III-B, the equations are optimized specifically for the proposed LE-DPAM technology utilizing CB028 and ABS as a conductive ink and a dielectric substrate, respectively. The equations have been modified to fit measured and simulated values taken at the center frequency of the operational bandwidth established by the SRF, to guarantee a variation of less than 5% from the near de capacitance value. A very

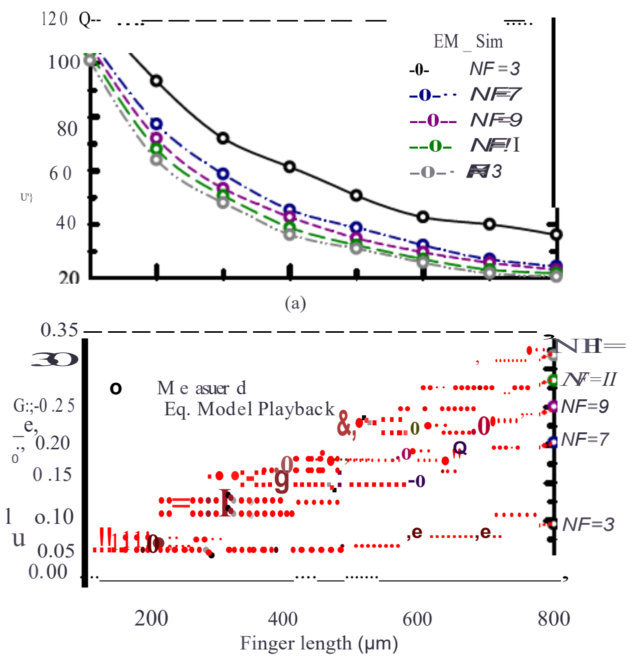

Fig. I6. (a) Simulated SRF for different finger length DFL and different number of fingers NF. (b) Equation-based prediction of capacitance plotted against the finger length (DH,} for different numbers of fingers NF (noted in the plot).

good agreement is observed between the equation model playback and the obtained capacitance values in the range of 0.0541.325 pF, with a maximum error of 1.1%.

The performance of the capacitors presented in this paper is compared with some obtained with other AM techniques, as well as with traditional GaAs MMIC processing in. Compared with other AM approaches, the high $Q$ values obtained with LE--DP AM are associated mainly with the effect of the laser processing on the walls of the conductor slots that increases the effective cond uctivity, as noted above. Note that the quality factor of the capacitor and its capac itance are inversely related, and both parameters are dependent on the materials and fabrication process.

## V. CONCLUSION

The results in this paper show that LE-DPAM enables the fabrication of lumped mm-wave components with high capacitance or inductance per unit area. The quality factors are, in general, better than those obtained with other **AM** techniques, and are reaching the performance obtained with GaAs **MMIC** process ing. Such passive componentsare important for the realization of RF front ends using AM. The LE-DPAM approach offers broad design freedom, where MMIC dies can be packaged and interconnected with multilayer passive elements, all using a single tool. These packages can be integrated into larger systems, to achieve structural electronics with a reduced size and weight. The overall achievable capacitance and inductance per unit area are bound by the geometry of the components and the materials. The proposed manufacturing technique can be adapted to achieve differen t geometries tlould offer better performance, and a higher permittivity material can be employed to increase the capacitance values.

## R EFE RENC ES


[I ] F. Cai, Y.-H. Chang, K. Wang, C. Zhang, B. Wang, and J. Papapolymerou, "Low-loss 3-D multilayer transmission lines and interconnecst fabricated by additive manufacturing technologies," *IEEE Trails. Mierow. Theory Techn.*, vol. 64, no. JO, pp. 3208- 3216 , Oct 2016.

[2] C. Mariotti, F. Alimenti, L. Roselli, and **M. M.** Tentzeris, "High-perfonnance RF devices and components on flexible cellulose substrate by vertically integrated additive manufacturing technologies," *IEEE Trails. Mierow. Theory Tech11.*, vol. 65, no. l , pp. 62- 71, Jan. 2017.

[3] G. McKerricher, **J.** G. Perez, and A. Shamim, "Fully inkjet printed RF inductors and capacitors us ing polymer dielectric and silver conductive ink with through vias," *IEEE Tr(lJls. Ele c tro 11 Device s* , vol. 62, no. 3, pp. 1002- 1009, Mar. 2015.

[4] E. A. Rojas-Nastrucci, T. Weller, V. L. Aida, C. Fan, and J. Papapolymerou, "A study on JD-printed coplanar waveguide with meshed and finite ground planes," in *Proc. 15th A11111i. IEEE Wireless Mierow. Techllol. Co11f ( WAMICON ),* Jun. 2014, pp. 1- 3.

[5] T. P. Ketterl *et al.,* "A 2.45 GHz phased array antenna unit cell fabricated using 3-D multi-layer direct digital manufacturing," *IEEE Tra11s. Mierow. Theory Teclu1.*, vol. 63, no. 12, pp. 4382-4394, Dec. 2015.

[6] N. Amal *et al.,* "3D multi-laye r additive manufacturing of a 2.45 GHz RF front end," in *IEEE MTT-S I11t. Mierow. Symp. Dig. (IMS ),* May 2015, pp. 1-4.

[7] R. A. Ramirez, D. Lugo, T. M. Weller, M. Golmohamadi , and J. Frolik, "Additive manufactured tripolar antenna system for link improvement in high multipath environments," in *Proc. IEEE fllt. Symp. A11te1111as Pro pag., USNC/URSI Nat. Radio Sci. Meeting* , Jul. 2017, pp. 2539- 2540.

[8] 1. Nassar, H. Tsang, and T. Weller, "3D printed wideband hannonic transceiver for embedded passive wireless monitoring", *Electro11. Lett.*, vol. 50, no. 22, pp. 1609-161l , 2014.

[9] E. A. Rojas-Nastrucci, R. Ramirez, D. Hawatmeh, D. Lan, J. Wang, and T. Weller, "Laser enhanced direct print additive manufacturing for mm-wave co mponents and packaging," in *Proc. 1111. Co11f El ectromag 11. Adv. Appl. ( ICEAA),* Verona, Italy, Sep. 2017, pp. 1531-1534.

[10] E. A. Rojas-Nastrucci *et aL,* "Characterization and modeling of K-band coplanar waveguides digitally manufactured using pulsed picosecond laser machining of thick-film conductive paste," *IEEE Tra11s. Mierow. Theory Teclul,* vo l. 65 , no. 9 , pp . 3 18 0---31 87 , Sep. 2017.

[11] R. A. Ramirez, D. Lan, J. Wang, and T. M. Weller, " MMIC packaging and on-chip low-loss lateral interconnection using additive manufacturing and laser machining," in *IEEE MTT-S /111. Mierow. Symp. Dig. (IMS ),* Honololu, Ill , USA, Jun. 2017, pp. 38--40.

[12] D. Hawatmeh and T. Weller, "2.4 GHz band pass filter architecture for direct print additive manufacturing," in *IEEE MTT-S Int. Mierow. Symp. Dig. (IMS),* Philadelphia, PA, USA, Jun. 2018, pp. 67- 70.

[13] E. A. Rojas-Nastrucci, R. A. Ramirez, and T. M. Weller, "Direct digital manufacturing of mm-wave vertical interconnects," in *Proc. 19th A1111u. IEEE Wireless Mierow. Technol. Co11f. ( WAMICON ),* Sand Key, FL, USA, Apr. 2018, pp. 1- 3.

[14] A. L. Vera-Lopez, E. A. Rojas-Nastrucci, **M .** Cordoba -Erazo, T. Weller, and J. Papapolymerou, "Ka-band characterization and RF design of acrynolitrile butadiene styrene (ABS)," presented at the IEEE MTT-S l nt. Mierow. Symp. Dig. (]MS), Phoenix, *AZ,* USA, 2015.

[15] R. A. Ramirez, D. Lan, E. A. Rojas-Nastrucci, and T. **M.** Weller, "Laser assisted additive manufacturing of CPW mm-wave interdigital capacitors," in *IEEE MTT-S fllt. Mierow. Symp. Dig. (IM,S)* Philadelphia, PA, USA, Jun. 2018, pp. 1553-1556.

[16] M. F. Cordoba-Erazo, E. A. Rojas-Nastrucci, and T. Weller, "Simultaneous RF electrical conductivity and topography mapping of smooth and rough conductive traces using microwave microscopy to identify localized variations," in *Proc. 16th Amiu. IEEE Wireless Mierow. Tec/1110/. Co11f. (WAMICON ),* Apr. 2015, pp. 1-4.

[17] I. Wolff, *Copla11ar Microwave I11tegrated Cir cuits* , 1st ed. Hoboken, NJ, USA: Wiley, 2006.

[18] M. Kang, J. Gil, and H. Shin, "A simple parameter extraction method of spiral on-chip inductors," *IEEE Trans. Electro11 Devices* , vol. 52, no. 9, pp. 1976--1981, Sep. 2005.

[19] T. H. Lee, *The Desig11 of CMOS Radio-Frequency I11t eg rated Circuits,* 2nd ed. Cambridge, MA, USA: Cambridge Univ. Press, 2003.

[20] D. M. Pozar, *Microwave E11gi 11ee ri11 g,* 2nd ed. Hoboken, NJ, USA: Wiley, 2004.

[21] J. Castro, E. A. Rojas-Nasrtucci, **A.** Ross, T. M. Weller, and J. Wang, "Fabrication, modeling, and application of ceramic-thermoplastic composites for fused deposition modeling of microwave com ponents," *IEEE Trans. Mierow. Theory Techn.,* vol. 65, no. 6, pp. 2073- 2084, Jun. 2017.

[22] H. A. Wheeler, "Simple inductance formulas for radio coils," *Proc. [11st. Radio Eng.,* vol. 16, no. 10, pp. 1398-1400, Oct. 1928.

[23] C. Nguyen, *Radio-Frequelcy llltegrated-Circuit Engineering.* Hoboken, NJ, USA: Wiley, 2015.

[24] S.-Y. Wu, C. Yang, W. Hsu, and L. Lin, "3D-printed microelectronics for integrated circuitry and passive wireless sensors," *Microsyst. Na11oe11g.,* vol. 1, Jun. 2015, Art. no. 15013.

[25] I. A. Ukaegbu, K. S. Choi, 0. Hidayov, J. Sangirov, T. W. Lee, and H. H. Park, "Small-area and high-inductance se mi-stacked spiral inductor with high Q factor," *!ET Microwaves, Antell/las Propag.,* vol. 6, no. 8, pp. 880---883, Jun . 2012.

[26] I. Wolf,f *Coplanar Microwave !11tegrated Circuits* . Hoboken , NJ, USA: Wiley, 2006.

[27] V. N. R. Vanukuru, "Millimeter -wave bandpass filter using high-Q conical inductors and MOM capacitors," in *Proc. IEEE Radio Freq. !11tegr. Circuits Symp. (RFIC),* May 2016, pp. 39--42.

[28] Y. H. Jung *et al.,* "High-performance green flexible electronics based on biodegradable cellulose nanofibril paper," *Nature Commun.,* vol. 6, May 2015, Art. no. 7170.

**Ramiro A. Ramirez** (S' 14) received the B.S. degree in electrical engineering from the Universidad de Carabobo, Valencia, Venezuela, in 2009, and the M.S. and Ph.D. degrees in electrical engineering from the University of South Florida, Tampa, FL, USA, in 2015 and 2018, respectively.

He is currently a Senior RF Design Engineer with Qorvo US, Inc., Greensboro, NC, USA. He holds two U.S. patents. His current research interests include developing additively manufactured systems for high multipath environments.

**Ed ua rd o A. Rojas-Nastru cci** (S' 12- M' l8 ) received the B.S. degree in electrical engineering from the Universidad de Carabobo, Valencia, Venezuela, in 2009, and the M.S. and Ph.D. degrees in electrical engineering from the University of South Florida, Tampa, FL, USA, in 2014 and 2017, respectively.

He joined Embry-Riddle Aeronautical University (ERAU), Daytona Beach, FL, USA, in 2017, where he is currently an Assistant Professor. He is also the Director of the Wireless Devices and Electromagnetics Laboratory, ERAU. He has over 27 peer-reviewed publications. He has two U.S. patents and three active U.S. patent applications. His current research interests include microwave/mm-wave circuit and antenna applications of additive manufactu ring, and RFID for wireless sensing.

Dr. Rojas-Nastrucci is member of the IEEE MTT-S Technical Committee 24. He is a Reviewer for the IEEE MTT-S TRANSACTIONS ON MICROWAVE T HEORY AND TECHNIQUES and the PROCEEDINGS OF THE IE EE .

**T hom as M. Welle r** (S '92 - M'95-S M'98- F' 18) received the Ph.D. degree in electrical engineering from The University of Michigan, Ann Arbor, Ml, USA.

From 1995 to 2018, he was a faculty member with the Electrical Engineering Department and a member of the Center for Wireless and Microwave Information Systems, University of South Florida, Tampa, FL, USA. He joined Oregon State University, Corvallis, OR, USA, in 2018, where he is currently a Professor and the Head of the School of Electrical Engineering and Computer Science. He has authored over 300 professional publications. He holds over 35 U.S. patents. His current research interests include RF/microwave applications of additive manufacturing, development and application of microwave materials, integrated circuits, and antenna design.